On the semiannual formation of large scale three-dimensional vortices at the stratopause

Terence J. O'Kane[1], Vassili Kitsios[2], Mark A. Collier[2]

[1]CSIRO Oceans and Atmosphere, Battery Point, Hobart, Tasmania, Australia
[2]CSIRO Oceans and Atmosphere, Aspendale, Melbourne, Victoria, Australia

Key Points:

- EOF analysis of the second matrix invariant of the velocity gradient tensor is applied to the shear zones about the tropical stratosphere.
- We identify large scale vortices near the tropical stratopause as reconstructed in the NASA MERRA-2 atmospheric reanalysis.
- The vortices form following the vernal and autumnal equinoxes at times when the westerly jet is maximal.

Corresponding author: Terence J. O'Kane, terence.okane@csiro.au

Abstract

An examination of the dynamics of the middle atmosphere as reconstructed in the NASA Modern-Era Retrospective analysis for Research and Applications, Version 2 (MERRA-2) reveals the formation of large scale three dimensional vortices in the tropical stratosphere following both the vernal and autumnal equinoxes at times when the jet associated with the westerly phase of the semiannual oscillation (SAO) is maximal and extra-tropical influences from planetary waves are weakest. An empirical orthogonal function (EOF) analysis of the second matrix invariant of the velocity gradient tensor applied to the shear zones about the SAO reveals statistically stationary wave-5 vortex structures that span more than 3200km in length and up to 40km in the vertical. Eliassen-Palm fluxes suggests the vortices are maintained by a combination of local (shear zones) and remote (vertically propagating tropical) sources of momentum. These large scale coherent features appear to be unique to the stratopause.

Plain Language Summary

Application of methods commonly employed in engineering fluid mechanics to visualise vortices are used to examine a recent state of the art reconstruction of the middle atmosphere. This analysis reveals huge vortical structures present during the equinoctal seasons in the region of the tropical stratopause. These semiannual coherent features appear to be unique to the middle atmosphere spanning up to 30° longitude at ±15° latitude corresponding to around 3200km in length and between 10 hPa and 0.1 hPa encompassing up to 40km in the vertical.

1 Introduction

The tropical middle atmosphere semiannual oscillation (SAO), observed in temperature and the zonal wind variations, was first discovered in radiosonde and rocketsonde measurements in the early 1960's (R. J. Reed, 1962). The SAO is evident from the upper levels of the stratosphere (stratopause) and throughout the mesosphere with very clear phase-locking to the annual cycle. The SAO dominates the variability about the stratopause (≈1 hPa) where easterly extreme wind speeds are typically reached following the December and June solstices and the westerly extreme winds after the equinoxes around April and October (Müller et al., 1997). The mean annual evolution of the stratopause SAO has been characterised using 20 years of rocketsonde observations at Ascension Island (8°S, 14°W) and Kwajalein (8°N, 167°E) as a Hovemölleŕ time-height diagram of the zonal wind between $20km$ and $60km$ in which the westerlies form in the lower mesosphere shortly after the solstices propagating downward with an average speed of 6-7km month^{-1} and reaching maximum average values in excess of $25ms^{-1}$ ($20ms^{-1}$) after the equinoxes in April (October) (Baldwin et al., 2001; Smith et al., 2017, 2020; Kawatani et al., 2020). The observed downward progression of the westerly acceleration phase of the SAO suggests a strong role for westerly Kelvin waves as being the source of the requisite momentum flux (R. Reed, 1965), and supported on theoretical grounds in terms of the interaction of a vertically-propagating Kelvin wave with the mean background flow (Dunkerton, 1979).

Hopkins (1975) first suggested a close coupling between the easterly phase of the SAO and planetary wave activity in the winter hemisphere arguing that, consistent with the theoretical work of Dickinson (1968), the stationary planetary waves of the winter hemisphere stratosphere would be absorbed about the critical line i.e., where the mean zonal wind is $0ms^{-1}$, near the equator producing an easterly zonal acceleration with little tendency for downward propagation. Hopkins (1975) further suggested that the stronger planetary wave activity in the Northern Hemisphere winter was the cause for the stronger variance in the monthly mean easterly tropical zonal winds after the January solstice ($\approx 40ms^{-1}$) in contrast to the June solstice ($\approx 20ms^{-1}$). On the basis of the Hopkins (1975) study, Holton (1975) proposed that the SAO results from the combined effects of a steady background source of westerly momentum due to Kelvin waves excited in the tropical troposphere as the cause of the westerly phase of the SAO where its downward propagation is indicative of dissipation of vertically propagating waves near critical layers. Using a two-dimensional atmospheric model for zonal mean temperature, winds and chemical constituent mixing ratios developed by Harwood and Pyle (1975), Gray and Pyle (1986) examined the additional westerly momentum required to successfully simulate the SAO double peak observed in low latitude satellite tracer distributions (N_2O and CH_4). In contrast, the easterly phase was hypothesised to arise from the annual cycle of easterly momentum due to vertically and equatorward propagating planetary waves of the winter hemisphere stratosphere being absorbed near the critical line in the tropics. As such, the stratospheric easterly phase arises due to mean advection of easterly momentum by the seasonally dependent meridional circulation, thus setting the semiannual period of the SAO.

Subsequent observational studies added further weight to the mechanism proposed by Holton (1975), showing that the transition from westerlies to easterlies occurs rather suddenly throughout a deep layer due to the easterly phase of the SAO being forced by the dissipation of horizontally traveling planetary waves (Hirota, 1980) and cross-equatorial advection of easterly winds by the residual mean meridional circulation (R. J. Reed, 1966; Meyer, 1970; Holton & Wehrbein, 1980; Dickinson, 1968; Meyer, 1970; van Loon et al., 1972; Belmont et al., 1974a, 1974b; Hopkins, 1975; Müller et al., 1997; Garcia et al., 1997; Garcia & Sassi, 1999; Hirota, 1978, 1980; Li et al., 2012). Additional observational studies of temperature and trace constituent data (Hirota, 1978, 1979; Bergman & Salby, 1994), combined with analysis based on the vertical component of the Eliassen-Palm (E-P) flux (Andrews et al., 1983), revealed short-period, equatorially trapped Kelvin waves with periods less than 2 days propagating vertically into the stratosphere are the most likely sources of the majority of the momentum required to generate both the quasi-biennial oscillation (QBO) and SAO (see also Sato and Dunkerton (1997)). Bergman and Salby (1994) used high resolution imagery of the global convective pattern to show that these short period waves are generated in geographical locations over the Indian Ocean to the western tropical Pacific and to a lesser extent over the African, and American continents. Theoretical and modeling studies, such as the one by Dunkerton (1979), showed that a Kelvin wave with sufficiently fast phase speed could propagate through the stratosphere with only modest attenuation and then be strongly absorbed in the region of very fast radiative damping near the stratopause.

Sassi and Garcia (1997) used spatial and temporal distributions of equatorial heating based on Bergman and Salby (1994) to successfully model a realistic SAO in the middle atmosphere. More generally, the stratopause SAO has been successfully simulated in a number of GCMs (Hamilton & Mahlman, 1988; Sassi et al., 1993; Jackson & Gray, 1994; Müller et al., 1997; Zülicke & Becker, 2017). This has allowed the mechanisms involved in driving the SAO to be examined in detail (at least within the context of the GCMs). That said, there is much to understand regarding the dynamics of the SAO and in particular the respective roles of planetary and gravity waves (Hamilton, 1998). Smith (2012) reviews the literature on the SAO in the broader context of the dynamics of the middle atmosphere - lower thermosphere (MLT) and in particular the variability and changes in direction of the zonal winds due to interactions with gravity waves. They make the point that, above 50km the details of the mean meridional circulation are difficult to measure (Smith et al., 2017) and that numerical models must be relied upon for the large scale wave driven motions of the middle atmopshere. Coherent temperature or "pancake" anomalies have been identified in the lower equatorial mesosphere (Hitchman et al., 1987) resulting from inertial instabilities (Harvey & Knox, 2019) and strong forcing of the subtropical mesosphere by large scale Rossby waves. For a recent detailed analysis of the momentum budget in the stratosphere, mesosphere, and lower thermosphere see the recent studies undertaken by Sato et al. (2018) and Yasui et al. (2018).

In the absence of direct observations of winds between 10 hPa (35km) and 0.01 hPa (80km), Smith et al. (2017) derived monthly zonally averaged tropical zonal winds in the middle atmosphere using the balance wind relationship from satellite geopotential height retrivals. They found easterly maxima near the solistices at 1.0 hPa, westerely maxima near the equinoxes at 0.1 hPa and easterly maxima near the equinoxes 0.01 hPa with the maxima significantly stronger during the first cycle, and importantly for this study, strongest near March at 0.1 and 0.01 hPa. While global climate model simulations of the zonal mean zonal winds near the stratopause generally reproduce the observed amplitudes and phases of the SAO there is some tendency for the models to be more westward than observations might indicate (Smith et al., 2020). Recent intercomparisons of reanalyses temperatures and winds through the SPARC reanalysis intercomparison project (S-RIP) (Long et al., 2017) reveal reasonable agreement amongst the more recent reanalyses (CFSR, MERRA, MERRA-2, JRA-55 and ERA-Interim) and for the zonal winds in the upper stratosphere. A detailed comparison of the zonal winds and temperature in the equatorial stratosphere and lower mesosphere in a number of reanalysed products to recent satellite SABER and MLS observations has been published by Kawatani et al. (2020). They find some significant differences in the variation and displacement of the equatorial zonal wind SAO amplitude maximum between the various reanalyses for heights above 1 hPa.

The structure of descending alternating easterly and westerly jets comprising the SAO and their associated shear zones suggests the possibility that large scale coherent structures might at times be present when the shear zones between the vertical easterly - westerly - easterly jet structure are sufficiently strong that vortical filaments are manifest within the confines of the westerly jet which acts as a waveguide. The main methods for the identification of three dimensional vortices are based on pointwise analysis of the velocity gradient tensor (Chakraborty et al., 2005). The characteristic shapes of vortical structures in turbulent flows, including regions of vorticity in the form of filaments, sheets, and blobs are a question of long- standing and intense interest. Vortex filaments are known to play an important role in the overall turbulence dynamics where local or point-wise methods of vortex identification typically are used to define a function that can be evaluated point-by-point and then classify each point as being inside or outside a vortex according to a criterion based on the point values (Hunt et al., 1988; Chong et al., 1990; Soria et al., 1994; Kitsios et al., 2011). Most local vortex identification criteria are based on the kinematics implied by the velocity gradient tensor, thereby making them Galilean invariant i.e. invariant to uniform rotations and translations. One of the most popularly used local criteria is the second matrix invariant of the velocity gradient tensor Q (Hunt et al., 1988). In order to isolate regions that might contain coherent vortical structures, we first calculate the velocity gradient tensor from the MERRA-2 reanalysis (Gelaro & Co-authors, 2017), then, following Soria et al. (1994), we calculate Q between 100 hPa and 0.01 hPa. Empirical orthogonal function (EOF) analysis is then applied to isolate regions of high Q variance and the corresponding vortical (positive Q) isosurface structures.

This paper is structured as follows. The MERRA-2 reanalysis is briefly described in section 2. We next characterise the SAO as represented in MERRA-2 in section 3 followed by the calculation of the velocity gradient tensor and the second invariant Q (section 4.1), and the EOFs of Q (section 4.2) and a case study of the observed vortical structures evident on April 1984 (section 4.3). A final summary is presented in section 5.

2 Data

We analyse the middle atmosphere using MERRA-2 data. MERRA-2 is an atmospheric reanalysis of the modern satellite era produced by the NASA Global Modeling and Assimilation Office (GMAO) (Gelaro & Co-authors, 2017). The processed daily and monthly averages used in this study are based on 3-hourly time averaged three-dimensional collections consisting of 361 latitudes, 576 longitudes and 72 levels. The height - pressure relationship to model level is displayed in (supplemental Figure 1). All analyses are performed on the full horizontal grid with calculations of the vortex structures restricted to the 38 levels above 100 hPa. MERRA-2 provides a multidecadal reanalysis whereby aerosol and meteorological (satellite radiances, microwave temperature, ATOVs etc) observations are jointly assimilated within a global data assimilation system. In addition to improved representations of cryospheric processes, MERRA-2 also includes several improvements to the representation of the stratosphere including ozone (total column, profiles from EOS Aura OMI). Importantly for the middle atmosphere, the gravity wave parameterization has been retuned to produce a model generated QBO rather than relying on one imposed through reanalysis tendencies to the wind and temperature fields. For a complete list of observations assimilated see table 1 of Gelaro and Co-authors (2017). Of relevance to our study, in the stratosphere at 10 hPa MERRA-2 has a negative bias of 20.3 Kelvin (K°) prior to the assimilation of AIRS radiances in 2002. These biases trend upward becoming positive in 2005. After 2005, assimilation of both MLS temperature retrievals (above 5 hPa) and GPSRO bending angle observations (up to approximately 10 hPa) begins in MERRA-2 such that after 2006, the biases have an average value of 0.2-0.3 K. Importantly for this study MERRA-2, resolves most of the middle atmosphere up to just below the mesospause at 0.01 hPa.

The detailed comparison of the representation of the equatorial stratopause SAO in the major reanalysis products that resolve the stratosphere to SABER and MLS observations by Kawatani et al. (2020) reveals MERRA and MERRA-2 to have very realistic zonal mean zonal wind amplitude and phase variations (their Figure 1) and climatological annual cycle for the zonal wind at around 1 hPa over the equator (their Figure 9) relative to other available reanalysis products which uniformly exhibit much weaker westerly equinoctal winds. It is on this basis we choose MERRA-2 as a valid representative data set for stratopause zonal wind variations. We will not discuss MERRA-2 further simply referring the reader to the relevant citation (Gelaro & Co-authors, 2017). MERRA-2 products are accessible online through the NASA Goddard Earth Sciences Data Information Services Center (GES DISC).

3 Characterising the semiannual oscillation in MERRA-2

In the following we summarise the general mechanism of the SAO easterly and westerly phases, as present in MERRA-2, in terms of the propagation of zonal winds over time and via the transfer of momentum. Figure 1 shows monthly averages of the U zonal winds averaged between 0°-360° longitude and 5°N-5°S latitude. The black contour shows zero average of winds. April and October are indicated by the pink and cyan vertical lines respectively. The downward propagation of the alternating easterly and westerly jets is evident as are their relative strengths.

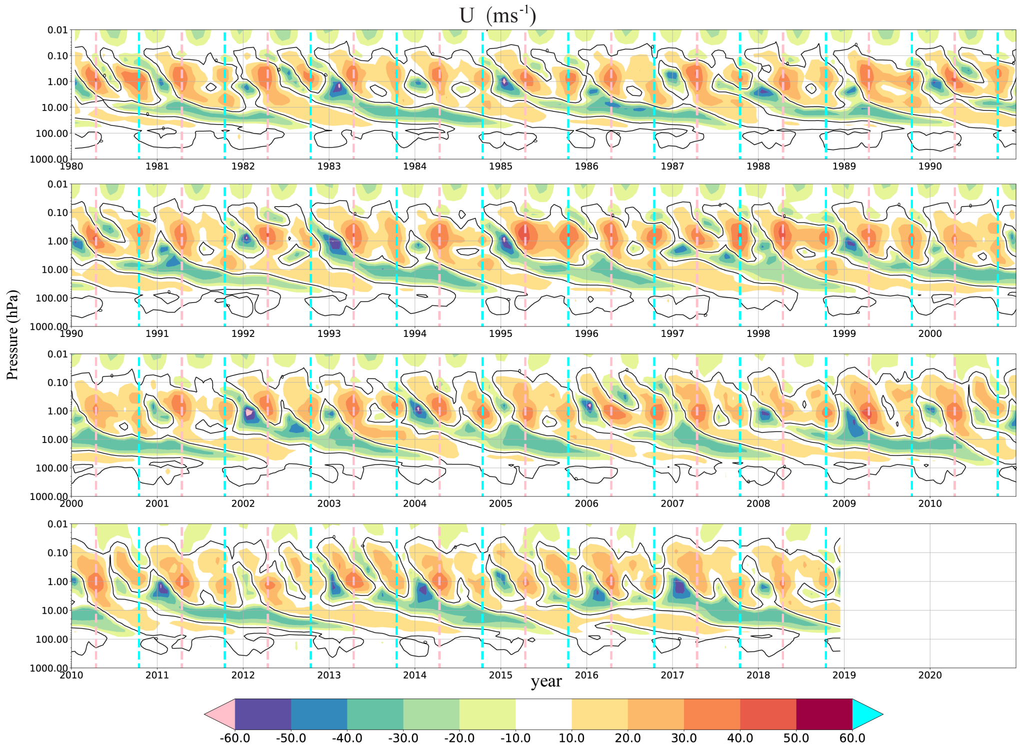

Figure 1. Monthly averages of the U zonal winds averaged between 0°-360° longitude and 5°N-5°S latitude. Black contour shows the critical line. April and October are indicated by the pink and cyan vertical lines respectively.

Eliassen-Palm (E-P) fluxes are calculated to examine the transfer of momentum from sources in the extratropics via the winter hemisphere and also tropical sources due to Kelvin and inertial gravity waves. The E-P flux provides a useful tool to describe wave propagation in mean zonal shear flows (Andrews et al., 1983). The E-P flux is defined as

$$\mathbf{F} = \{F_\phi, F_p\} = \{-a\cos\phi\overline{U'V'}, fa\cos\phi\frac{\overline{V'\theta'}}{\theta_p}\} \tag{1}$$

where a is the Earth's radius, f is the Coriolis force, ϕ is the latitude, θ the potential temperature, the zonal and meridional velocities (U, V). Eddy flux terms are computed from the daily zonal anomalies and the product is zonally and then time averaged over the period 1980-2018. $\theta_p = \frac{\partial\theta}{\partial p}$ is calculated as the time-mean, zonal mean value of θ. When the E-P flux vector points upward, the meridional heat flux dominates; when the vector points in the meridional direction, the meridional flux of zonal momentum dominates. The divergence of the E-P flux is proportional to the eddy potential vorticity flux and when zero i.e. $\bigtriangledown\cdot\mathbf{F} = 0$, thermal wind balance is maintained (Edmon et al., 1980).

Climatological E-P fluxes were calculated using daily U, V and θ data over the period 1980-2018 . In Figure 2 shading is the flux divergence with negative values (red) indicating absorption and positive (blue) shading indicative of the production of momentum. See supplementary Figure 2 for all other months. Black contours are the climatological winds whereas the critical line corresponds to the magenta contour line. Following Coy et al. (2017), all quantities (E-P fluxes and U zonal winds) have been divided (normalised) by the associated 1980-2018 standard deviation at each latitude and level. This has the two-fold benefit of 1) not requiring the usual adhoc scaling of quantities in the vertical, for example due to the magnitude differences of E-P flux vector components (Taguchi & Hartmann, 2006) and 2) highlighting exceptional values e.g. individual months or years as discussed in the folowing sections. In addition, the vectors below 100 hPa have been appropriately thinned for display purposes.

For the solstices, the mean temperature gradient between the summer and winter poles is a maximum at the stratopause resulting in a single thermal cell characterised by rising (sinking) motion in the summer (winter) hemisphere, a compensating flow from the summer to winter hemisphere, where a strong zonal asymmetry arises due to the injection of momentum from the winter hemisphere. Thus for the solstices momentum flux into the equatorial stratopause is not balanced by equal contributions from both hemispheres required to drive the equatorial westerly jet which is necessary to generate the required shear and to act as a waveguide for the formation of coherent vortex structures. Hence the easterley phase of the SAO is structurally unable to support the existence of large scale coherent vortices.

For the easterly SAO phase, the Hovemoller plot of the MERRA-2 zonal winds U in the middle atmosphere reveals the relative strengths of the easterly SAO maxima following the respective solstices (Figure 1). Specifically, the maximum zonal winds are in excess of $30ms^{-1}$ and occur in January and August at $\approx$ 1 hPa following the December and June solstices. In January, the easterly jet is at a maximum then decays over the first half of the year before re-establishing with typically significantly weaker maximum values after the June solstice. Climatalogical E-P flux vectors during the solstices (see December and June climatologies in supplemental Figure 2) reveal extratropical planetary waves propagating into the tropics from the winter hemisphere whereas E-P flux divergences show deposition of (easterly) momentum due to the dissipation of the aforementioned planetary waves driving wave forcing and mean advection. This is consistent with the general mechanism for the easterly phase of the SAO first proposed by Holton (1975). As the SAO easterly phase relies on planetary wave forcing and mean momentum advection, it is strongly coupled to the annual cycle and specifically to the winter hemisphere.

Due to the seasonal reversal of the mean zonal and meridional winds the equinoctal and solstitial seasons differ substantially. Specifically, the radiatively driven mean meridional circulation in the equinoctal season is characterised by upward motion at the equator and corresponding subsidance near the poles with the Coriolis torque generating mean westerlies in both hemispheres (see Figure 2). The associated momentum flux due to the observed mean meridional overturning circulation (Figure 2) closely matches that described by Gray and Pyle (1986) with a horizontal flux of momentum into the equatorial westerly jet at the stratopause ($\approx$ 1 hPa - 50 km). The westerly SAO phase (Figure 1) is characterised by a pronounced zonal symmetry about the equator and strong mean westerly jets in excess of $35ms^{-1}$. For the months of April and October immediately after the equinoxes, the westerly SAO jet, centered near 1 hPa, is maximal with zonally symmetric momentum fluxes and divergence (Figure 2). The equinoctal E-P flux vectors are consistent with the induced meridional overturning circulation from satellite observations of tracer distributions described in Figure 3 of Gray and Pyle (1986). E-P flux divergence indicates westerly momentum sources (positive) where the equatorial jet forms acting to maintain and enhance the jet. The E-P fluxes indicate the equatorial stratopause regions are the primary source of momentum driving the westerly equatorial stratopause jet, with little evidence of systematic inter-hemispheric momentum flux due to extratropical planetary waves. Tropical sources due to Kelvin and inertial gravity waves are clearly evident during the westerly phase. These sources of momentum are associated with tropical convection and are thought to be responsible for generating the westerly phase via interaction of the mean flow with vertically propagating internal gravity waves and large-scale equatorial waves generated in the lower atmosphere. The climatological westerly jet has a generally downward propagation from 0.1 hPa to about 1 hPa and is strongest in April with a secondary maxima in October. Our results are generally supportive of the hypothesis of Holton (1975) that high frequency Kelvin waves, with periods from 2 to 4 days, originating in the troposphere propagate unhindered into the middle atmosphere where they are absorbed about the critical line as the major source of momentum during the westerly phase.

4 Stratopause vortex structures

An examination of the middle atmosphere Q in all months (not shown) revealed vortical structures are only evident in the stratopause SAO westerly phase and are most coherent after the equinoxes. These structures are highly dependent on the westerly jet being sufficiently strong, requiring velocities in excess of $35ms^{-1}$, and where sufficient shear is present in the gradients at the upper and lower boundaries of the SAO. We shall show that preferential conditions for these vortex structures to occur are where there is a well developed easterly jet present in the vicinity of 0.1 hPa above the westerly SAO jet and when the QBO is strongly easterly.

4.1 Calculation of Q

Following (Chong et al., 1990; Soria et al., 1994; Chakraborty et al., 2005) we define the velocity gradient tensor A_{ij} in terms of symmetric $S_{ij} = S_{ji}$ and anti-symmetric $W_{ij} = -W_{ji}$ parts where,

$$A_{ij} = \partial U_i/\partial x_j = S_{ij} + W_{ij} \tag{2a}$$

and

$$S_{ij} = (\partial U_i/\partial x_j + \partial U_j/\partial x_i)/2 \tag{2b}$$

$$W_{ij} = (\partial U_i/\partial x_j - \partial U_j/\partial x_i)/2 \tag{2c}$$

are the rate of strain and the rate of rotation tensors respectively. The $U_{i=1,2,3}$ indices are the zonal and meridional velocities (U, V) in meters per second (ms^{-1}) and ω the Lagrangian rate of change of pressure with time in units of pascals per second $(Pa\ s^{-1})$. The $x_{i=1,2,3}$ indices are latitude and longitude (ϕ, λ) in meters (m) and isobaric pressure level p in Pa respectively. The eigenvalues γ of A_{ij} satisfy the characteristic equation

$$\gamma^3 + P\gamma^2 + Q\gamma + R = 0, \tag{2d}$$

where the matrix invariants are

$$P = -\operatorname{Tr}[A] = -S_{ii} \tag{2e}$$

$$\begin{aligned} Q &= \frac{1}{2}(P^2 - \operatorname{Tr}[A^2]) = \frac{1}{2}(P^2 - S_{ij}S_{ji} - W_{ij}W_{ji}) \\ &= \begin{vmatrix} \frac{\partial U}{\partial \phi} & \frac{\partial U}{\partial \lambda} \\ \frac{\partial V}{\partial \phi} & \frac{\partial V}{\partial \lambda} \end{vmatrix} + \begin{vmatrix} \frac{\partial U}{\partial \phi} & \frac{\partial U}{\partial p} \\ \frac{\partial \omega}{\partial \phi} & \frac{\partial \omega}{\partial p} \end{vmatrix} + \begin{vmatrix} \frac{\partial V}{\partial \lambda} & \frac{\partial V}{\partial p} \\ \frac{\partial \omega}{\partial \lambda} & \frac{\partial \omega}{\partial p} \end{vmatrix} \end{aligned} \tag{2f}$$

Tr is the trace, Q has units of s^{-2}, and

$$R = -\left|A\right| \tag{2g}$$

where || defines the determinant.

For turbulence in three dimensional flows, large scale coherent eddies decay as vorticity diffuses out in convergence zones defined where there is irrotational straining and strong divergence and convergence of streamlines. In other words, the magnitude of the straining defined by $S_{ij}S_{ji}$ is large compared to the magnitude of the rate of rotation, with regions of elongation $S_{ij}S_{jk}S_{ki} > 0$ and flattening $S_{ij}S_{jk}S_{ki} < 0$ (Hunt et al., 1988). For incompressible flows, where the first flow invariant $P = -S_{ii} = 0$, it follows that the second invariant $Q = (W_{ij}W_{ij} - S_{ij}S_{ij})/2$. This means that large negative values of Q are indicative of regions where the strain dominates the rotation whereas for large positive values rotation dominates strain. In the results presented here, we have defined Q in terms of the zonal and meridional velocities (U, V) and $\omega = \frac{Dp}{Dt}$ the Lagrangian rate of change of pressure with time, hence for constant model grid pressure levels, ω depends only on the vertical wind velocity and the change in pressure with height, from which it follows that the interpretation of Q is exactly as for 3D turbulence.

4.2 EOFs of Q

In calculating EOFs of Q, we first construct daily anomalies w.r.t. the climatological month i.e. $Q'(\phi, \lambda, p, t) = Q(\phi, \lambda, p, t) - \overline{Q}(\phi, \lambda, p)$. We then construct spatial anomalies Q'' from the zonal average $\breve{Q}$ as $Q''(\phi, \lambda, p, t) = Q'(\phi, \lambda, p, t) - \breve{Q}(\phi, p, t)$. These anomalies are then normalized by the spatial and temporal standard deviation σ of Q'' at each pressure level i.e. $\hat{Q}(\phi, \lambda, p, t) = Q''(\phi, \lambda, p, t)/\sigma(p)$. In the current study, vortex structures will be represented by isosurfaces of EOFs of Q. Normalizing by the spatio-temporal standard deviation allows us to then rescale the EOF patterns before calculating the iso-surfaces of interest i.e. $Q_i^{eof}(\phi, \lambda, p) = \hat{Q}_i^{eof}(\phi, \lambda, p) \times \sigma(p)$.

The 3D structures for the leading EOFs 1 & 2 of Q for April (Figure 3) and October (Figure 4) reveal a distinct wave-5 pattern with opposite sign about the equator due to the change of sign in the meridional velocity gradient. These EOFs are in quadrature. The corresponding April 2D EOFs at 0.62 hPa i.e., through the middle of the westerly jet, have explained variances of 2.9% and 2.4% respectively. The structures are less coherent between 200°E and 300°E which is the region where the westerly jet of the SAO is consistently weak and where the mean zonal wind velocities, are considerably less than the maximum mean values as indicated by the $35ms^{-1}$ mean U contour line (yellow) in the top-down perspectives. As for April, the leading pair of 3D-EOFs of October Q are confined to a region where the background zonal U wind exceeds $35ms^{-1}$. The structures would again appear to be close to a hemispheric wave-5 pattern if the westerly jet was strong enough to support it.

The April 3D-EOFs 3 & 4 (supplemental Figure 3) form a large scale wave-4 pattern with individual structures in excess of 40° longitude spanning 20°N to 20°S. The corresponding 2D-EOFs 3 & 4 explain 2.3% & 2.0% of the Q variance respectively at 0.62 hPa. All 4 leading 3D-EOFs for April display noticeable asymmetry being larger and more coherent south of the equator. October 3D EOFs 3 & 4 (supplemental Figure 4) appear to be wave-6 and do not display the North - South asymmetries present for April. October 3D-EOFs 3 & 4 are considerably noisier than for April, a reflection of the weaker background flow and reduced shear zones.

4.3 April 1984 case study

In order to show that the vortical Q structures are not simply statistical, we now focus exclusively on the westerly phase of the SAO associated and the particular month of April 1984. This date was chosen as the vortical structures are particlularly evident with no filtering required, however, a number of other dates could have been chosen. An examination of the mean April 1984 E-P fluxes (Figure 5) shows close similarities to the climatological April previously discussed. We see absorption of momentum about the critical line associated with the easterly QBO phase and some evidence of flux into the tropics as the SH transitions to winter. There is evidence of eddy forcing (positive E-P flux divergence) in the shear regions between the easterly QBO and the westerly SAO ($\approx$ 10 hPa), and between the westerly SAO and the weak easterly jet near 0.1 hPa. Most interesting is to consider the anomalous flux w.r.t. the climatological April. Here we see an intense highly localized source of momentum in the shear zone i.e. +ve E-P flux divergence at 10 hPa, with a closeby corresponding region of absorption into the westerly SAO jet on the opposite side of the critical line between ±20° latitude.

Having identified the regions of shear between the respective easterly and westerly jets as significant sources (and sinks) for momentum, we now examine the aforementioned

Q flow invariant. The April 1984 isosurfaces of the monthly mean U winds and Q between 0.01 hPa and 100 hPa are shown in Figure 6. Here the westerly positive phase of the SAO ($30ms^{-1}$ green isosurface) is wedged between the easterly mesosphere jet between 0.01 hPa and 0.1 hPa and the easterly phase of the QBO between 10 hPa and 60 hPa ($5ms^{-1}$ purple isosurfaces). In the regions of shear between the respective jets, Q isosurfaces are largely unorganised and noisy. These are the regions corresponding to large amplitude anomalous E-P fluxes (Figure 5). The large scale coherent positive Q isosurfaces i.e. vortices, are, as for the leading April EOFs, entirely contained within the westerly jet centred about 1 hPa and occur only at latitudes where the jet exceeds $30ms^{-1}$. In common with the April EOFs 1 & 2, these structures span up to 30° longitude at ±15° latitude corresponding to around 3200km in length and between 10 hPa and 0.1 hPa encompassing up to 40km in the vertical.

5 Summary

Vortex structures associated with Q manifest only during the SAO westerly phase and only where the westerly jet reaches speeds in excess of $35ms^{-1}$. Similar wind velocities are necessary to form the shear zones at the jets upper and lower boundary. As such the vortices are most coherent during March-April and less evident during October. The Q structures manifest on given dates within the equinoctal month(s) with wave numbers between 4-7 but are typically wave-5, resembling the leading statistically stationary 3D-EOF Q patterns. Our analysis indicates that the vortices are maintained by a combination of local (shear zones) and remote (vertically propagating tropical) sources of momentum. Although not directly discussed here, there is evidence that the phase relationship between the QBO and SAO directly influences the strength of the shear zone at the lower boundary of the stratopause SAO during its westerly phase with consequences for the resulting Q vortices.

The emergence of the vortex structures during the westerly SAO phase and their dependence on the jet strength and shear at the boundaries indicates a rich flow geometry allowing methods commonly applied to analyse turbulent shear flows to be fruitfully employed. The scale and extent of these vortical structures, structures that appear to be unique to the stratopause, is remarkable. While the mechanisms of the SAO have been generally understood for quite some time, many of the details remain to be quantified, particlularly the spectrum of Kelvin and inertial gravity waves required to generate sufficient momentum to drive the westerly phase. Despite not explicitly resolving gravity waves due to our reduced temporal resolution, our E-P flux analysis is broadly consistent with the recent detailed analysis of Sato et al. (2018). They emphasise the complicated roles of E-P flux divergences and nonlinear dynamics during the equinoctal seasons, clear motivation for further exploration of the unique coherent structures appearing near the stratopause.

Observational evidence for the existence of the vortex structures described here might in principle be derived from long lived satellite trace gas distributions, such as N_2O, from instruments such as the Microwave Limb Sounder (MLS) on the Earth Observing System Aura satellite launched in July 2004. While the scientifically useful range of the Aura/MLS N_2O data is from 100 to 1 hPa (Khosrawi et al., 2013) the detection of equinoctal vortices at the stratopause may be difficult but perhaps not impossible due to the size of the structures in question. Similar limitations on the effective vertical extent of observations apply to Kelvin wave signatures in stratospheric trace constituents from MLS however the observational basis for the important role of fast Kelvin waves on the dynamics of the stratosphere is well established (Salby et al., 1984; Gray & Pyle, 1986; Mote et al., 2002; Mote & Dunkerton, 2004; Feng et al., 2007).

Finally it remains to verify the existence of equinoctal stratopause vortices in other reanalyses and if possible observational data and to develop the corresponding linear instability analysis to better understand the mechanisms by which these structures might manifest.

Acknowledgments

The authors appreciate helpful discussions with Adam Scaife and Jorgen S. Frederiksen. We thank Ajay Limaye and support from the NCI Visualisation lab for generating Figure 6. This work was supported by the Australian Commonwealth Scientific and Industrial Research Organisation (CSIRO) Decadal Climate Forecasting Project (https://research.csiro.au/dfp). Datasets for this research are available in these in-text data citation references: (Gelaro & Co-authors, 2017).

References

Andrews, D. G., Mahlman, J. D., & Sinclair, R. W. (1983). Eliassen-Palm diagnostics of wave-mean flow interaction in the GFDL "SKYHI" general circulation model. *J. Atmos. Sci.*, *40*, 2768–2784.

Baldwin, M. P., Gray, L. J., Dunkerton, T. J., Hamilton, K., Haynes, P. H., Randel, W. J., ... Takahashi, M. (2001). The Quasi-Biennial Oscillation. *Reviews of Geophysics*, *39*, 179–229.

Belmont, A. D., Dart, D. G., & Nastrom, G. D. (1974a). Periodic variations in stratospheric zonal wind from 20-65km, at 80°n to 70°s. *Quart. J. Roy. Meteor. Soc.*, *100*, 203–211.

Belmont, A. D., Dart, D. G., & Nastrom, G. D. (1974b). Variations of stratospheric zonal winds, 20-65 km, 1961-1971. *J. Appl. Meteor.*, *14*, 585–594.

Bergman, J. W., & Salby, M. L. (1994). Equatorial wave activity derived from fluctuations in observed convection. *J. Atmos. Sci.*, *51*, 3791–3806.

Chakraborty, P., Balachandar, S., & j. Adrian, R. (2005). On the relationships between local vortex identification schemes. *J. Fluid Mech.*, *535*, 189–214. doi: 10.1017/S0022112005004726

Chong, M. S., Perry, A. E., & Cantwell, B. J. (1990). A general classification of three-dimensional flow fields. *Phys. Fluids A.*, *2*, 765–777. doi: 10.1063/1.857730

Coy, L., Newman, P. A., Pawson, S., & Lait, L. R. (2017). Dynamics of the disrupted 2015/16 quasi-biennial oscillation. *J. Clim.*, *30*, 5661–5674.

Dickinson, R. E. (1968). Planetary Rossby waves propagating vertically through weak westerley wind wave guides. *J. Atmos. Sci.*, *25*, 984–1002.

Dunkerton, T. J. (1979). The role of the Kelvin wave in the westerly phase and the semiannual zonal wind oscillation. *J. Atmos. Sci.*, *36*, 32–41.

Edmon, H. J., Hoskins, B., & McIntyre, M. (1980). Eliassen-Palm cross sections for the troposphere. *J. Atmos. Sci.*, *37*, 2600–2616.

Feng, L., Harwood, R. S., Brugge, R., O'Neil, A., Froidevaux, L., Schwartz, M., & Waters, J. W. (2007). Equatorial kelvin waves as revealed by EOS Microwave Limb Sounder observations and European Centre for Medium-Range Weather Forecasts analyses: Evidence for slow Kelvin waves of zonal wave number 3. *J. Geophys. Res.*, *112*, D16106. doi: 10.1029/2006JD008329

Garcia, R. R., Dunkerton, T. J., Lieberman, R. S., & Vincent, R. (1997). Climatology of the semiannual oscillation of the tropical middle atmosphere. *J. Geo-*

phys. Res., *102*, 26019–26032.

Garcia, R. R., & Sassi, F. (1999). Modulation of the mesospheric semiannual oscillation by the quasibiennial oscillation. *Earth Planets Space*, *51*, 563–569.

Gelaro, R., & Co-authors. (2017). The Modern-Era Retrospective Analysis for Research and Applications, Version 2 (MERRA-2). *J. Clim.*, *30*, 5419–5454. doi: 10.1175/JCLI-D-16-0758.1

Gray, L. J., & Pyle, J. A. (1986). The semi-annual oscillation and equatorial tracer distribution. *Quart. J. R. Met. Soc.*, *112*, 387–407.

Hamilton, K. (1998). Dynamics of the tropical middle atmosphere: A tutorial review. *ATMOSPHERE-OCEAN*, *36*, 319–354.

Hamilton, K., & Mahlman, J. D. (1988). General circulation model simulation of the semiannual oscillation of the tropical middle atmosphere. *J. Atmos. Sci.*, *44*, 3212–3235.

Harvey, V. L., & Knox, J. A. (2019). Beware of inertial instability masquerading as gravity waves in stratospheric temperature perturbations. *Geophys. Res. Lett.*, 1740–1745. doi: 10.1029/2018GL081142

Harwood, R. S., & Pyle, J. A. (1975). A two-dimensional mean circulation model for the atmosphere below 80km. *Quart. J. R. Met. Soc.*, *101*, 723–748.

Hirota, I. (1978). Equatorial waves in the upper stratosphere and mesosphere in relation to the semiannual oscillation of the zonal wind. *J. Atmos. Sci.*, *35*, 714–722.

Hirota, I. (1979). Kelvin waves in the equatorial middle atmosphere observed by Nimbus 5 SCR. *J. Atmos. Sci.*, *36*, 217–222.

Hirota, I. (1980). Observational evidence of the semiannual oscillation in the tropical middle atmosphere. *Pure Appl. Geophys.*, *118*, 217–238.

Hitchman, M. W., Leovy, C. B., Gille, J. C., & Bailey, P. L. (1987). Quasi-stationary zonally asymmetric circulations in the equatorial lower mesosphere. *J. Atmos. Sci.*, *44*, 2219–2236.

Holton, J. R. (1975). *The dynamic meteorology of the stratosphere and mesosphere* (Vol. 15). American Meteorological Society.

Holton, J. R., & Wehrbein, W. M. (1980). A numerical model of the zonal mean circulation of the middle atmosphere. *Pure Appl. Geophys*, *118*, 284–306.

Hopkins, R. H. (1975). Evidence of polar-tropical coupling in upper stratospheric zonal wind anomalies. *J. Atmos. Sci.*, *32*, 712–719.

Hunt, J. C. R., Wray, A. A., & Moin, P. (1988). Eddies, stream, and convergence zones in turbulent flows. *Proceedings of the Summer Program*, *Center for Turbulent Research Report CTR-S8*, 193–208.

Jackson, D. R., & Gray, I. J. (1994). Simulation of the semiannual oscillation of the equatorial middle atmosphere using the extended UGAMP general circulation model. *Q. J. R. Meteorol. Soc.*, *120*, 1559–1588.

Kawatani, Y., Hirooka, T., Hamilton, K., Smith, A. K., & Fujiwara, M. (2020). Representation of the equatorial startopause semiannual oscillation in global atmospheric reanalyses. *Atmos. Chem. Phys.*, *20*, 9115-9133. doi: 10.5194/acp-20-9115-2020

Khosrawi, F., Müller, R., Urban, J., Proffitt, M. H., Stiller, G., Kiefer, M., ... Murtagh, D. (2013). Assessment of the interannual variability and influence of the qbo and upwelling on tracer–tracer distributions of n2o and o3 in the tropical lower stratosphere. *Atmos. Chem. Phys.*, *13*, 3619–3641. doi: 10.5194/acp-13-3619-2013

Kitsios, V., Cordier, L., Bonnet, J.-P., Ooi, A., & Soria, J. (2011). On the coherent structures and stability properties of a leading edge separated aerofoil with turbulent recirculation. *J. Fluid Mech.*, *683*, 395–416.

Li, T., Liu, A. Z., Lu, X., Li, Z., Franke, S., Swenson, G. R., & Dou, X. (2012). Meteor-radar observed mesospheric semi-annual oscillation (SAO) and quasi-biennial oscillation (QBO) over Maui, Hawaii. *J. Geophys. Res.*, *117*, D05130. doi: 10.1029/2011JD016123

Long, C. S., Fujiwara, M., Davis, S., Mitchell, D. M., & Wright, C. J. (2017). Climatology and interannual variability of dynamics variables in multiple reanalyses evaluated by the SPARC Reanalysis Intercomparison Project (S-RIP). *Atmos. Chem. Phys.*, 14593–14629. doi: 10.5194/acp-17-14593-2017

Meyer, W. D. (1970). A diagnostic numerical study of the semiannual variation of the zonal wind in the tropical stratosphere and mesosphere. *J. Atmos. Sci.*, *27*, 820–830.

Mote, P. W., & Dunkerton, T. J. (2004). Kelvin wave signatures in stratospheric trace constituents. *J. Geophys. Res. Atmospheres*, *109*, D03101. doi: 10.1029/2002JD003370

Mote, P. W., Dunkerton, T. J., & Wu, D. (2002). Kelvin waves in stratospheric temperature observed by the microwave limb sounder. *J. Geophys. Res.*, *107*, 4218. doi: 10.1029/2001JD001056

Müller, K. M., Langematz, U., & Pawson, S. (1997). The stratopause semiannual oscillation in the Berlin troposphere-stratosphere-mesosphere GCM. *J. Atmos. Sci.*, *54*, 2749–2759.

Reed, R. (1965). The quasi-biennial oscillation of the atmosphere between 30km and 50km over Ascension Island. *J. Atmos. Sci.*, *22*, 331–333.

Reed, R. J. (1962). Some features of the annual temperature regime in the tropical stratosphere. *Mon. Weather Rev.*, *90*, 211–215.

Reed, R. J. (1966). Zonal wind behaviour in the equatorial stratosphere and lower mesosphere. *J. Geophys. Res.*, *71*, 4223–4233. doi: 10.1029/JZ071i018p04223

Salby, M. L., Hartmann, D. L., Bailey, P. L., & Gille, J. C. (1984). Evidence for equatorial Kelvin modes in Nimbus-7 LIMS. *J. Atmos. Sci.*, *41*, 220-235.

Sassi, F., & Garcia, R. R. (1997). The role of equatorial waves forced by convection in the tropical semiannual oscillation. *J. Geophys. Res.*, *54*, 1925–1942.

Sassi, F., Garcia, R. R., & Boville, B. A. (1993). The stratopause semiannual oscillation in the NCAR Community Climate Model. *J. Atmos. Sci.*, *50*, 3608–3624.

Sato, K., & Dunkerton, T. J. (1997). Estimates of momentum flux associated with equatorial kelvin and gravity waves. *J. Geophys. Res.*, *102*, 26247–26261.

Sato, K., Yasui, R., & Miyoshi, Y. (2018). The momentum budget in the stratosphere, mesosphere, and lower thermosphere. Part I: Contributions of different wave types and in situ generation of Rossby waves. *J. Atmos. Sci*, *75*, 3613–3633. doi: 10.1175/JAS-D-17-0336.1

Smith, A. K. (2012). Global dynamics of the MLT. *Surv. Geophys.*, *33*, 1177–1230. doi: 1007/s10712-9196-9

Smith, A. K., Garcia, R. R., Moss, A. C., & Mitchell, N. J. (2017). The semiannual oscillation of the tropical zonal wind in the middle atmosphere derived from satellite geopotential height retrivals. *J. Atmos. Sci.*, *74*, 2413–2425.

Smith, A. K., Holt, L. A., Garcia, R. R., Anstey, J. A., nad N. Butchart, F. S., Osprey, S., ... Yoshida, K. (2020). The equatorial startospheric semiannual oscillation and time-mean winds in QBOi models. *Quart. J. R. Met. Soc.*, 1–17. doi: 10.1002/qj.3690

Soria, J., Sondergaard, R., Cantwell, B. J., Chong, M. S., & Perry, A. E. (1994). A study of the fine-scale motions of incompressible time-developing mixing layers. *Phys. Fluids*, *6*(2), 871–884.

Taguchi, M., & Hartmann, D. L. (2006). Increased occurrence of stratospheric sudden warmings during El Niño as simulated by WACCM. *J. Atmos. Sci.*, *19*, 324–332.

van Loon, H., Labitzke, K., & Jenne, R. J. (1972). Half-yearly waves in the stratosphere. *J. Geophys. Res.*, *77*, 3846–3855.

Yasui, R., Sato, K., & Miyoshi, Y. (2018). The momentum budget in the stratosphere, mesosphere, and lower thermosphere. Part II: The in situ generation of gravity waves. *J. Atmos. Sci*, *75*, 3635–3651. doi: 10.1175/JAS-D-17-0337.1

Zülicke, C., & Becker, E. (2017). Relation between equatorial mesospheric wind anomalies during spring and middle atmosphere variability modes. *SOLA*, *13A*, 31–35. doi: 10.2151/sola.13A-006

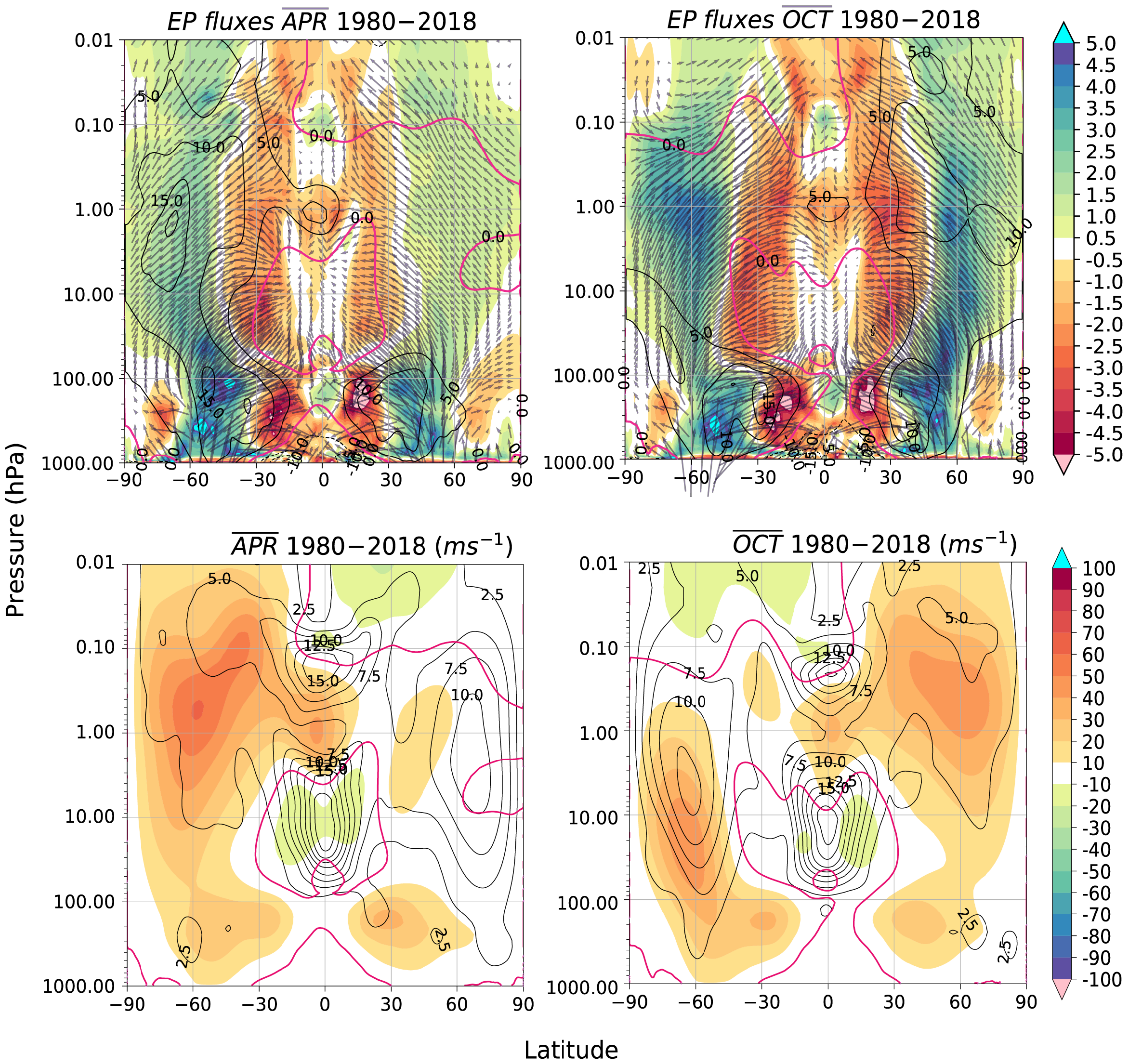

Figure 2. Left column: April and right column: October E-P flux calculations. (upper row) Climatological E-P fluxes, calculated using daily U, V and T data over 1980-2018. Shading is the flux divergence with positive (negative) values indicating westerly (easterly) sources of momentum. Black contours the climatological winds. Negative U values are dashed and zero corresponds to the magenta contour. All quantities (E-P fluxes and U zonal winds) have been divided by the 1980-2018 standard deviation. The vectors below 100 hPa have been appropriately thinned for display purposes. (lower row) Shading indicates the monthly climatological (1980-2018) U winds zonally averaged between 0°-360° longitude. Negative (positive) wind values indicate easterly (westerly) flow. Black contours are the corresponding standard-deviations in ms^{-1}.

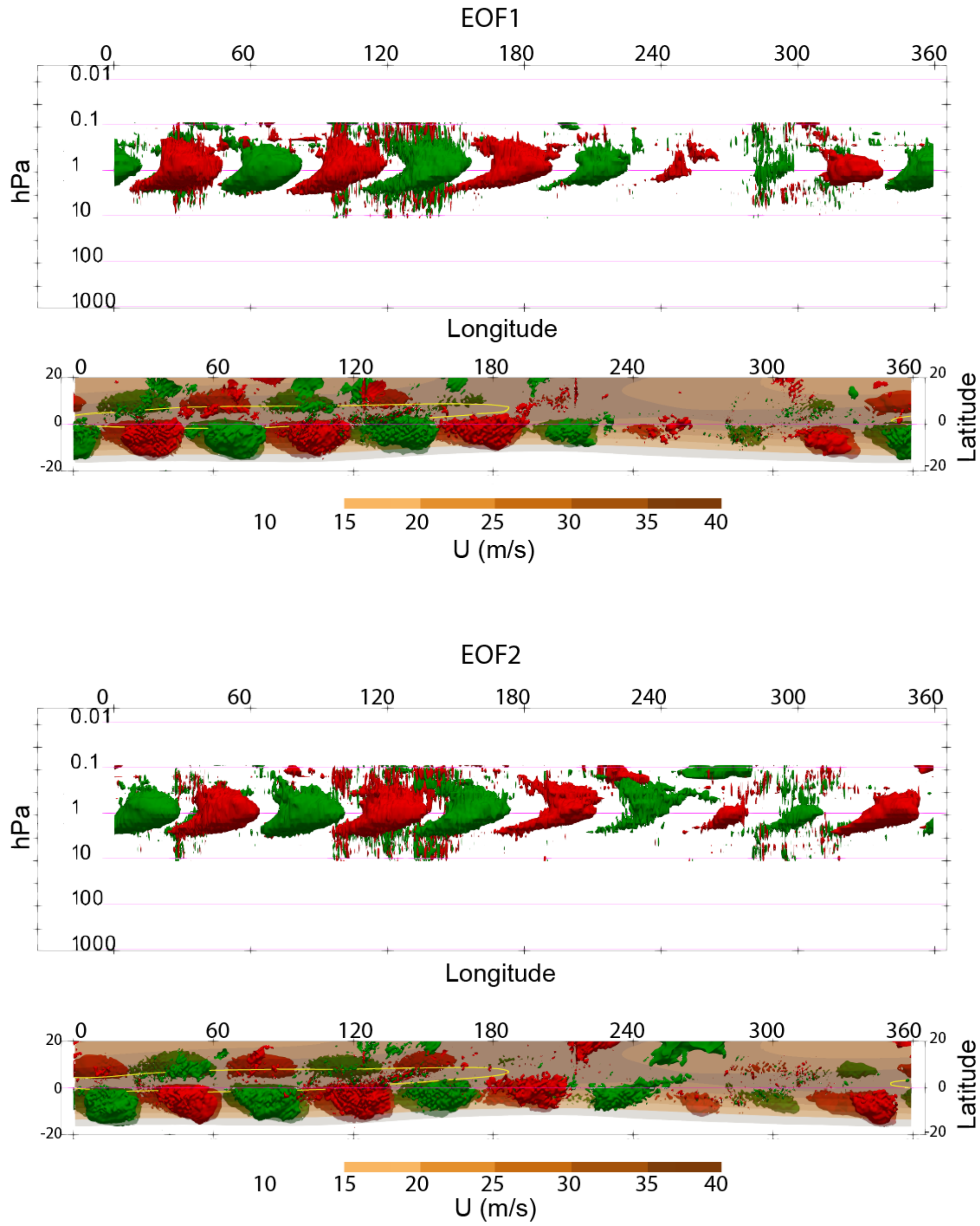

Figure 3. The leading 2 3D-EOFs of Q based on daily anomalies for April w.r.t. the climatological month viewed from the South and top-down. Positive (negative) Q values are indicated in red (green). Q isosurfaces correspond to $\pm 1.5e^{-11}$. The climatological U zonal wind velocities are indicated by the shaded background in the top-down view where velocities range from 15-40ms^{-1} with colouring in 5ms^{-1} increments indicated by the colour bar. The yellow contour indicates the boundary between the 30-35ms^{-1} & 35-40ms^{-1} climatological U zonal wind velocities. The opacity of the climatological U zonal wind vaues has been reduced in order to better see the structure below the 0.62 hPa level from the top down aspect panels.

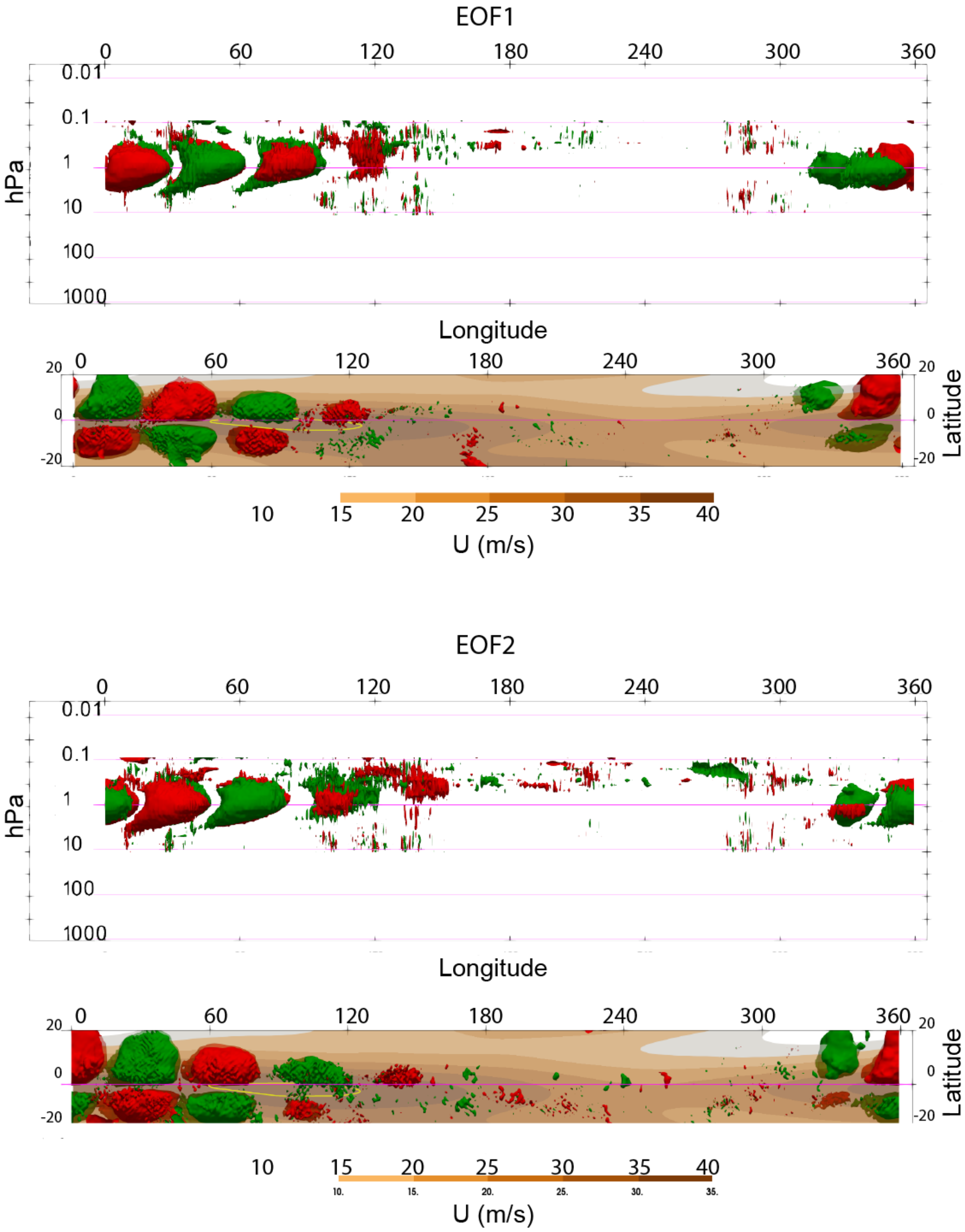

Figure 4. The leading two 3D-EOFs of Q based on daily anomalies for October. Velocities greater than $30ms^{-1}$ are identified by the yellow contour line. All other parameters are as for Figure 3.

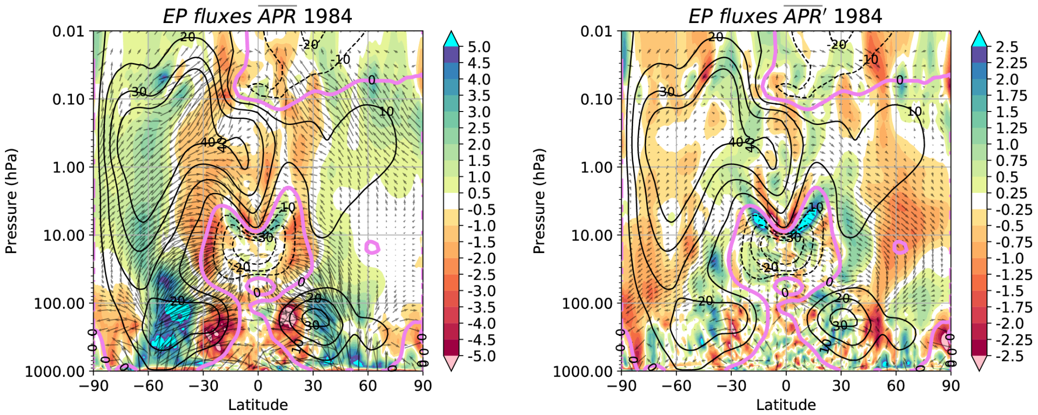

Figure 5. April 1984 monthly E-P fluxes (arrows) and flux divergence (shaded). Left panel is the average for April 1984, the right panel is the anomaly relative to long term 1980-2018 mean. Anomalies are normalised by the local standard deviation for the month. Black contours are respecitve monthly mean U zonal winds, and the zero contour (critical line) is shown in magenta (ms^{-1}).

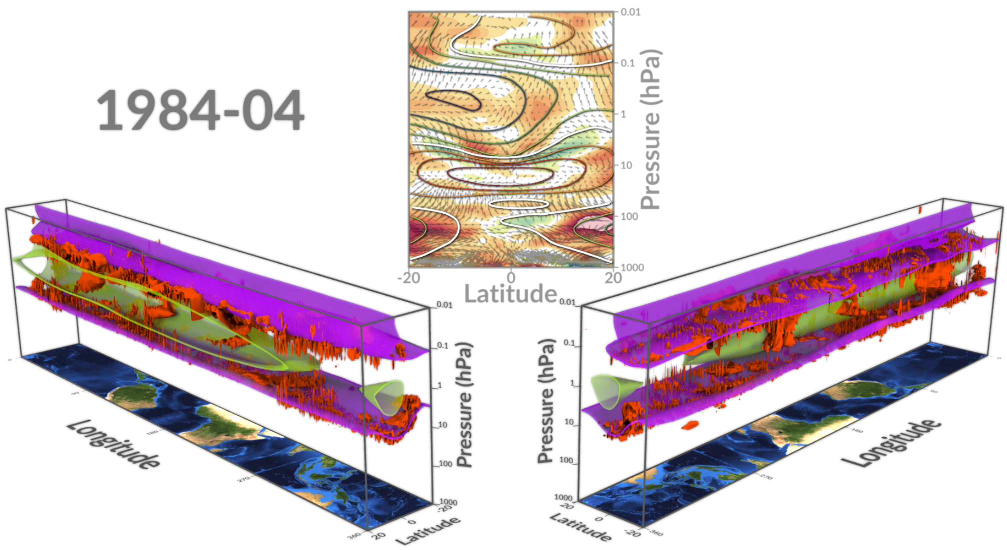

Figure 6. Isosurfaces of Q (positive 1.5e-11) and U (easterly $5ms^{-1}$ (magenta) and westerly $30ms^{-1}$ (green)) for April 1984. Q below 100 hPa has been greyed-out. Isosurfaces are identified between 0.01 hPa and 10 hPa. The middle insert panel displays April 1984 monthly E-P fluxes (arrows) and flux divergence (shaded) between 20°S and 20°N with the critical line shown as the white contour.